Laser-driven cylindrical compression of targets for fast electron transport study in warm and dense plasmas

B. Vauzour,[1] F. Pérez,[2] L. Volpe,[3] K. Lancaster,[4] Ph. Nicolaï,[1] D. Batani,[3] S. D. Baton,[2] F. N. Beg,[5] C. Benedetti,[6] E. Brambrink,[2] S. Chawla,[5] F. Dorchies,[1] C. Fourment,[1] M. Galimberti,[4] L. A. Gizzi,[7] R. Heathcote,[4] D. P. Higginson,[5] S. Hulin,[1] R. Jafer,[3] P. Köster,[7] L. Labate,[7] A. J. MacKinnon,[8] A. G. MacPhee,[8] W. Nazarov,[9] J. Pasley,[10] C. Regan,[1] X. Ribeyre,[1] M. Richetta,[11] G. Schurtz,[1] A. Sgattoni,[6] and J. J. Santos[1,a)]

[1]*Centre Lasers Intenses et Applications (CELIA), CNRS, CEA, Université Bordeaux 1, 33405 Talence Cedex, France*
[2]*LULI, École Polytechnique, CNRS, CEA, UPMC, 91128 Palaiseau Cedex, France*
[3]*Dipartimento di Fisica, Università di Milano-Bicocca, Milano 20126, Italy*
[4]*Central Laser Facility, Rutherford Appleton Laboratory, Didcot, United Kingdom*
[5]*Department of Mechanical and Aerospace Engineering, University of California, San Diego, La Jolla, California 92093-0411, USA*
[6]*Dipartimento di Fisica, Università di Bologna, Bologna, Italy*
[7]*Intense Laser Irradiation Laboratory at INO—CNR, Pisa, Italy*
[8]*Lawrence Livermore National Laboratory, Livermore, California 94550, USA*
[9]*University of St. Andrews, School of Chemistry, Fife KY16 9ST, United Kingdom*
[10]*Department of Physics, University of York, York YO10 5DD, United Kingdom*
[11]*Dipartimento di Ingegneria Meccanica, Università di Roma Tor Vergata, Roma, Italy*

(Received 24 January 2011; accepted 25 March 2011; published online 28 April 2011)

Fast ignition requires a precise knowledge of fast electron propagation in a dense hydrogen plasma. In this context, a dedicated HiPER (High Power laser Energy Research) experiment was performed on the VULCAN laser facility where the propagation of relativistic electron beams through cylindrically compressed plastic targets was studied. In this paper, we characterize the plasma parameters such as temperature and density during the compression of cylindrical polyimide shells filled with CH foams at three different initial densities. X-ray and proton radiography were used to measure the cylinder radius at different stages of the compression. By comparing both diagnostics results with 2D hydrodynamic simulations, we could infer densities from 2 to 11 g/cm^3 and temperatures from 30 to 120 eV at maximum compression at the center of targets. According to the initial foam density, kinetic, coupled (sometimes degenerated) plasmas were obtained. The temporal and spatial evolution of the resulting areal densities and electrical conductivities allow for testing electron transport in a wide range of configurations. © *2011 American Institute of Physics*. [doi:10.1063/1.3578346]

I. INTRODUCTION

In the context of inertial confinement fusion (ICF), the concept of fast ignition (FI) is based on a rapid ($\sim$10 – 20 ps) deposition of a high amount of energy ($\sim$20 kJ) in a precisely located small volume, the so-called hot-spot, within a compressed Deuterium–Tritium (DT) shell. Several approaches for creating this hot-spot have been investigated in the past years.[1,2] The most known one features a high intensity laser-generated electron beam as an ignitor (electron FI).[1] Here, the fast electron beam, generated out of the compressed core, has to propagate over some 100 μm from the critical density surface to the compressed DT shell,[3–5] where the electrons must efficiently deposit their energy. Crucial issues of this particular scheme consist in the laser-to-electron conversion efficiency and in the electron transport through a highly overdense plasma.

To understand both points, numerous experiments were realized using solid targets[6–15] and a few with 1D laser-compressed targets.[18–20] These pioneering works lead to the establishment of scaling laws for the laser-to-electron energy conversion efficiency,[7,9,10] the electron beam current average velocity,[6] and divergence.[11,12,15,16] Other experiments were devoted to measure the range, the collimation of these electrons, and the way they lose their energy while propagating through solid samples, either foils,[8,9,13,14,17] wire targets,[21,22] or 1D-compressed foils.[18,19,23] Nonetheless, using solid or even 1D-compressed targets strongly limits the area of investigation to low temperatures (<10 eV) and moderate densities (<5 g/cm^3), which are far from the plasma parameters of the compressed core of a driven ICF target (100 g/cm^3, 300 eV). In this context, laser-driven shock compression in 2D cylindrical geometry, in direct[24] or indirect drive,[25] is a promising technique for creating higher density and temperature plasmas, suitable for the next step of fast electron beam transport studies.

We report on an experimental work addressing two goals. The first one, presented in this article, consisted in studying the cylindrical compression of plastic targets in order to determine their temperature and density evolution during the compression. The second goal, presented elsewhere,[26,27] was devoted to the understanding of fast electron transport, generated by an intense laser beam, inside such compressed plasmas. We aimed to propagate the fast

a)Author to whom correspondence should be addressed. Electronic mail: Santos.Joao@celia.u-bordeaux1.fr.

electrons in plasmas having different thermodynamic properties as those met in FI fusion targets, either in terms of the degeneracy and coupling levels of a compressed DT core, or in terms of the temperature and density levels of the imploded plasma between the fast electron source (near the critical surface) and the compressed core. These plasma parameters were tuned by changing the initial density of the targets or the delay between the compression and the intense laser beams. This way, we tested plasmas with different conductivities producing different regimes of electron transport. The design of the cylindrical targets was optimized using the 2D hydrodynamic code CHIC (Code d'Hydrodynamique et d'Implosion du CELIA) from CELIA[28,29] according to the VULCAN laser characteristics. Two diagnostics were used for the compression monitoring: x-ray and proton radiography.

The paper is organized as follows: we introduce the experimental setup in Sec. II, the radiative-hydrodynamic code used to design and interpret the experiment in Sec. III, and present the results of x-ray radiography in Sec. IV. The experimental results are compared to the hydrodynamic simulations to infer plasma parameters in Sec. V.

II. EXPERIMENTAL SET-UP

A. Description of the laser and target configuration

The experiment was performed on the VULCAN Nd:glass ($\lambda = 1.053\,\mu$m) laser facility at the Central Laser Facility of the Rutherford Appleton Laboratory (RAL) in the United Kingdom. Four long-pulse (LP) laser beams (4×70 J, 1 ns at $\lambda/2$) were used to radially compress cylindrical targets (see Fig. 1). The four LP beams were symmetrically distributed around the cylindrical wall of the targets and focused using *hybrid* phase plates. The *top hat* spots sizes were 150 μm FWHM (full width at half maximum) giving a maximum intensity on target of 3.10^{14} W/cm^{-2}. The four LP laser beams were synchronized with a 50 ps accuracy.

The targets were composed of a 200 μm long, 220 μm diameter, and 20 μm thick hollow polyimide cylinder (with a density $\rho_{poly} = 1.1$g/cm^3), called *target shell*, filled with CH polymerized at three different initial densities ($\rho_0 = 0.1$, 0.3, and 1 g/cm^3), called *target core*. The cylinders were closed on both sides by 20 μm thick Ni and Cu foils placed, respectively, at the front and at the rear side. For the fast electron propagation study (not described here) a tube-shaped plastic-coated gold shield was stuck onto the Ni foil to protect it from the ablated plasma created by the LP lasers beams (see Fig. 1).

B. Diagnostics setup

The x-ray side-on radiography[30,31] diagnostic was mainly devoted to the characterization of the plasma parameters (density and temperature) of the 1 g/cm^3 targets at different stages of the compression.

A short pulse (SP) laser beam (10 ps, 160 J at $\lambda = 1.064\,\mu$m) was focused on a 25 μm thick Ti foil placed at $d = 10$ mm from the target. The focal spot was 20 μm diameter and the laser intensity on the foil 5.10^{18} W/cm^{-2}. The fast electron population created by the laser propagates into the solid target and generates Bremsstrahlung as well as line radiation from atoms, including inner-shell recombination lines like K_α-radiation. These x-rays transversally probed the cylinder during the compression. The transmitted x-ray K_α-radiation (Ti-$K_\alpha \approx 4.5$ keV) was selected via a spherically bent quartz crystal (Quartz 203, $2d = 2.749$ Å, $R_c = 380$ mm) at the first order Bragg incidence ($\theta_{Bragg} \sim 89.5^\circ$) located at a distance $L_1 = 210$ mm from the target,[32] as sketched in Fig. 2. The cylindrical target was imaged on the detector (Imaging Plate BAS-TR) located at $L_2 \sim 2$ m away from the crystal. The total magnification of the imaging system was $\gamma_{x-ray} = 10.7$ and the spatial resolution, depending on the crystal quality, the x-ray source size, the detector efficiency, and most importantly on the noise level, has been estimated to $\Delta x \sim 20\,\mu$m on target. Both values were experimentally measured by imaging a calibrated grid placed at the target chamber center. The foam filling the polyimide cylinders was doped with 30% of Cl (in mass) to increase its x-ray absorption and enhance the contrast of the x-ray radiography images. A variable delay τ was introduced between the SP and LP laser beams in order to probe the target at different compression stages ($0 < \tau < 3.5$ ns). The x-ray time of flight can be considered negligible compared to the laser jitter (0.1 ns) and the value $\tau = 0$ is taken as the beginning of the LP laser beams interaction with the target.

A transverse point-projection proton radiography diagnostic[33,34] was also implemented to monitor the compression of the 0.1 g/cm^3 targets. The proton backlighter source was obtained using an other short pulse (SP) laser beam focused on a 20 μm thick gold foil. The energy of the proton thus generated was in the range of 1–10 MeV. More details about the setup of this diagnostic can be found in Ref. 37.

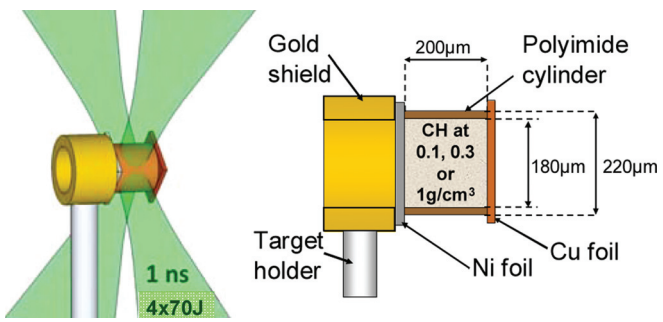

FIG. 1. (Color online) Schematics of the compression with the four long pulse beams (left) and of the cylindrical target (right).

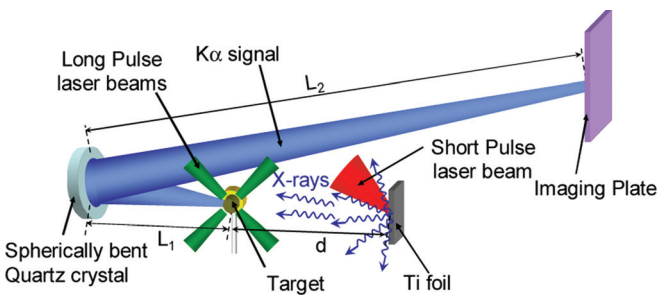

FIG. 2. (Color online) X-ray radiography setup.

III. HYDRODYNAMIC SIMULATIONS OF THE IMPLOSION

For both the experiment design and interpretation, cylindrical implosions are simulated using the radiative-hydrodynamic code CHIC (Refs. 28 and 29). It includes two-dimensional axisymmetric hydrodynamics based on a cell-centered Lagrangian scheme, electron and ion conduction, thermal coupling, and detailed radiation transport. In our case, the ionization and opacity data are tabulated assuming a local thermodynamic equilibrium (LTE), depending on the plasma parameters. The equations of state implemented in the code are based on a QEOS model[35] or SESAME (Ref. 36) tables. Laser propagation, refraction, and collisional absorption via inverse Bremsstrahlung are described by a 3D ray tracing algorithm. The cylindrical compression was simulated for the different targets, modeling the shell by a 1 g/cm^3 CH hollow cylinder filled with CH foam at the three different initial densities ($\rho_0 = 0.1$, 0.3, and 1 g/cm^3). The spatial profile of each $2\omega_0$ LP laser beam is Gaussian shaped, $I_{laser} \sim e^{-(r/r_0)^2}$, with $r_0 = 80\,\mu m$. The pulse temporal shape is 1 ns flattop with a rising time of 200 ps. The density and temperature 2D maps were computed for each target during its compression. The computation has been realized for laser energies 4×30, 4×48, and 4×70 J to take into account possible errors in the measurement of the experimental laser energy, in energy losses by the focusing optics, in the shape of the focal spots and in the way the laser absorption is numerically described.

IV. EXPERIMENTAL RESULTS

Figure 3(b) displays a typical x-ray radiography of the cylinder at $\tau = 2.2$ ns, next to, for comparison, a photography of the target before the shot [Fig. 3(a)]. One can clearly see a compression of the target. X-ray transmission profiles are extracted from radiographies for different delays τ by doing a lineout of the compressed part of the cylinder, as indicated by the white arrows in Fig. 3(b). Experimental radii (HWHM) are estimated by fitting these profiles with supergaussian functions of fourth order (for early times, i.e., when the cylinder's boundaries are still sharp) or Gaussian functions (close to the stagnation time, i.e., when the density gradients are less steep).

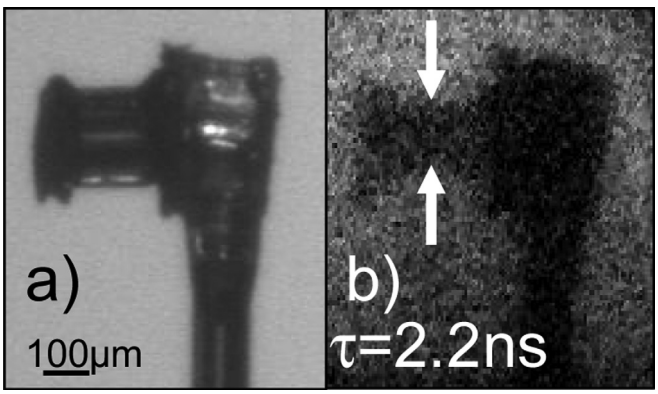

FIG. 3. (a) Photography of the target (1g/cc polymerized CH + 30% Cl doping in mass) before compression and (b) x-ray radiography of the same target during compression (at $\tau = 2.2$ ns). The white arrows highlight the compression region of the target. Both images have the same spatial scale.

Figure 4 presents the radius measurements (red triangles) of $\rho_0 = 1\ g/cm^3$ CH targets doped with 30% mass of Cl atoms at different stages of the compression. These experimental values are corrected on the widening due to the limited resolution of the imaging system: $HWHM_{corrected} = \sqrt{HWHM^2 - \Delta x^2}$. The curves in Fig. 4 show the radii deduced from calculations of x-ray transmission through the simulated target density profiles for different LP laser beam energies: 4×30, 4×48, and 4×70 J. X-ray transmissions are computed by assuming a laminar flow of x-rays transversally probing the imploding cylinder at different times. The region where one expects a transmission drop due to the Cl doping is the core–shell border. Because the temperature is not very high in this region, one can assume cold opacities for the calculation of x-ray transmission. The compressed target was modeled by time-dependent 2D density maps obtained from CHIC hydrodynamic simulations (see Fig. 7 in Sec. V). As stated in Sec. III, the compression laser energy is varied in the simulations in order to find the best match for the experimental points. The best agreement is found for 4×48 J. In this case, the maximum compression occurs at $\tau = 2.5 \pm 0.1$ ns (stagnation time), which is in fair agreement with experimental values (red triangles).

For comparison it is also presented the radial evolution of the denser zone (corresponding to the high density central part, as mentioned in Fig. 5) estimated directly from density profiles. The radius deduced from x-ray transmission profiles does not correspond to the compressed zone size. This is mainly due to the Cl doping.

The effect of the Cl doping in the target core is demonstrated in Fig. 5. Here, the simulated radial x-ray transmission profiles are shown for doped (dark-blue solid lines) and nondoped (blue dotted lines) $\rho_0 = 1\ g/cm^3$ targets, respectively (a) at the stagnation time $\tau = 2.5$ ns (i.e., at maximum compression), and (b) at $\tau = 3$ ns. We recall that these

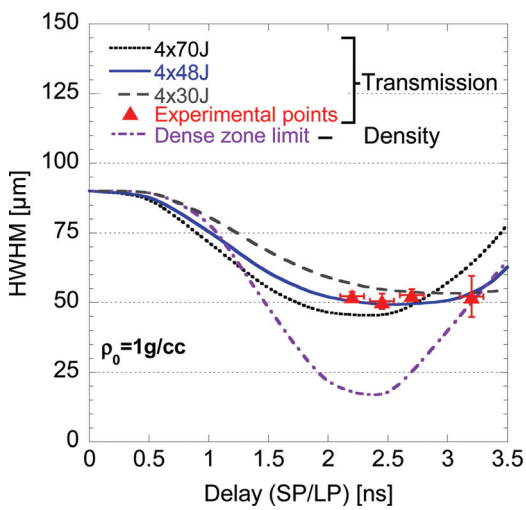

FIG. 4. (Color online) Evolution of the target radius measured by x-ray radiography ($HWHM_{corrected}$) for 1 g/cm^3 targets with 30%-mass Cl doping (red triangles), compared to simulated x-ray transmission profile radii for three different LP laser beam energies: 4×30 (gray dashed line), 4×48 (blue solid line), and 4×70 J (black dotted line). The CH denser zone radius given by the hydrodynamic simulation is also represented (dotted dashed purple line).

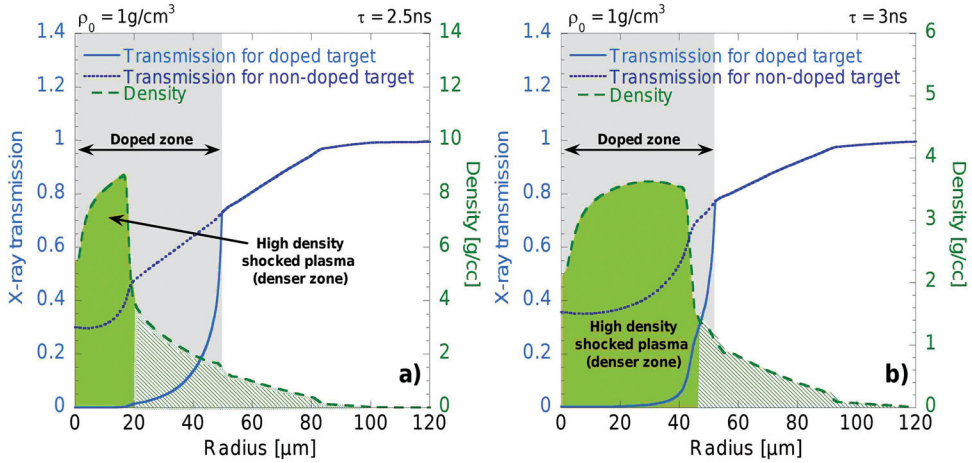

FIG. 5. (Color online) Simulated transmission profiles at $\tau = 2.5$ ns (left) and $\tau = 3$ ns (right) for $\rho_0 = 1\,\mathrm{g/cm^3}$ targets, doped with 30% Cl in mass (blue solid lines) or nondoped (blue dotted lines). The corresponding simulated density profiles are also plotted (green dashed lines). The gray background zones identify the zones containing Cl doping.

targets have a CH core and a polyimide shell of almost identical initial densities and that there is no Cl doping in the shell. The gray background zones identify the extent of the CH core, i.e., the zones including the Cl doping. One can notice the dopant Cl atoms improve the contrast ratio between the typical core and shell transmissions. The percentage of Cl doping was fixed to 30%-mass to guarantee a good transmission contrast (theoretical contrast: $C_{\mathrm{th}} \equiv T_{\max}/T_{\min} \approx 80$) between the core and the imploding shell. Experimentally the obtained contrast C_{exp} was only 2, partly due to the presence of a background noise covering the radiography. When comparing to the density profiles (dashed green lines) for times around the target stagnation, the compressed zone diameter is considerably smaller than the CH core size (corresponding to the doped zone size): at $\tau = 2.5$ ns [Fig. 5(a)] the compressed zone radius is $\approx 20\,\mu$m (HWHM) and the radius deduced from the x-ray transmission profile is $\approx 50\,\mu$m. For times before and after the stagnation the difference is much smaller, $\approx 5\,\mu$m (HWHM), as it is shown in Fig. 5(b) for $\tau = 3$ ns. These differences, that are important for $1.2\,\mathrm{ns} < \tau < 3\,\mathrm{ns}$ (see also Fig. 4), can be explained by the heated plasma expansion: It is indeed only at $\sim\tau = 1.2$ ns (i.e., at the end of the laser pulse) that the rarefaction front reaches the CH core producing important density inhomogeneities in the Cl-doped zone, which makes the transmission profiles significantly different from the density profiles. After stagnation, the shock rebounds and tends to homogenize the density. The density plateau thus generated becomes increasingly broad (but less dense) and ends up, at $\tau \sim 3 - 3.5$ ns, in including all the CH plasma, i.e., the entire Cl-doped area. In fact, without Cl doping one could hope to measure the real size of the compressed zone only at times close to the maximum compression. But in this case the limited transmission contrast ($C_{\mathrm{th}} \approx 2.3$) would induce large measurement uncertainties. The use of the doping allows for measuring the size of the CH core with a good accuracy for any τ and can be easily linked to hydrodynamic simulations via x-ray transmission profile calculations.

The results about the proton radiography of 0.1 g/cm^3 targets are reported by Volpe *et al.*[37] The experimental results are, in this case, compared to hydrodynamic simulations coupled to Monte–Carlo simulations assuming a laser-on-target energy of $4 \times (45 \pm 5)$ J as for the x-ray radiography. A good agreement is found (cf. Fig. 14 from Ref. 37) meaning that hydrodynamic simulations are reliable for this energy. However, it is important to notice that protons are subject to scattering and energy loss in the target. In the plasmas analyzed here, this effect may strongly degrade the spatial resolution of the diagnostic and, therefore, it should be taken into account in the simulations and experiments.

V. HYDRODYNAMIC EVOLUTION OF THE TARGETS

Good agreement between the results from hydrodynamic simulations and the experimental measurements reported in Previous section (cf. Fig. 4, and Fig. 14 from Ref. 37) provides confidence in the capacity of the hydrodynamic code to estimate the target density and temperature at any time of compression.

Figure 6 shows the mesh flow (r-τ) diagrams given by the hydrodynamic simulations for 4×48 J of laser energy on target. The red curves represent the boundary between the core and the shell. For $\rho_0 = 0.1\,\mathrm{g/cm^3}$ [Fig. 6(a)], the core radius is $\approx 15\,\mu$m at the stagnation and is equal to $50\,\mu$m for 1 g/cm^3 targets [Fig. 6(c)]. The corresponding temporal evolution of the core density and temperature averaged over the entire CH core is shown in Figs. 6(d)–6(f). The peak mean density and peak mean temperature are achieved at the stagnation times $\tau = 1.9$, 2.15, and 2.5 ns, respectively for $\rho_0 = 0.1$, 0.3, and 1 g/cm^3 targets. These are coincident with the minimum core radius in the (r-τ) diagrams. These values fairly agree with the experimental results deduced, respectively, from proton radiography of $\rho_0 = 0.1\,\mathrm{g/cm^3}$ targets and from x-ray radiography of 1 g/cm^3 targets. The mean temperature and density decrease with ρ_0 for all the three targets. Therefore, compression is more efficient in the case of the 0.1 g/cm^3 target where the mean peak density at stagnation is 40 times greater than the initial density. This has to be compared to those obtained for 0.3 g/cm^3 and 1 g/cm^3 targets where the achieved compression are only 13 and 3 times, respectively. In return, the stagnation is longer for denser targets: It lasts $\approx$0.3, $\approx$0.5, and $\approx$1.5 ns, for $\rho_0 = 0.1$, 0.3, and 1 g/cm^3, respectively.

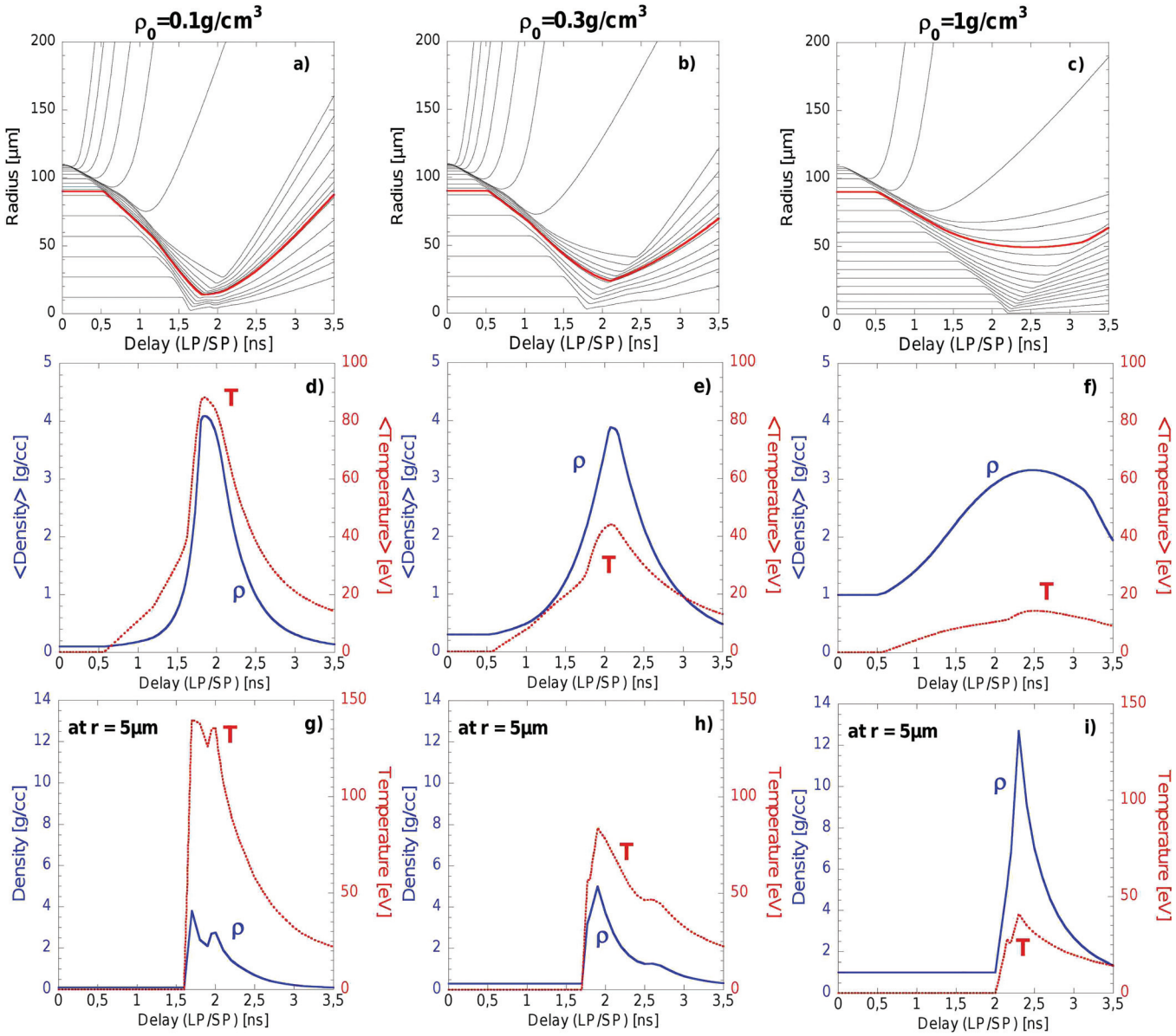

FIG. 6. (Color online) Hydrodynamic simulations mesh flow diagrams for (a) $\rho_0 = 0.1\,\mathrm{g/cm^3}$, (b) 0.3 $\mathrm{g/cm^3}$, and (c) 1 $\mathrm{g/cm^3}$ targets assuming 4×48 J of laser energy: The red curves represent the limit between the core and the shell. The plots below are the respective simulated temporal evolutions of the CH core density (blue solid lines) and temperature (red dotted lines), averaged over the entire CH core material for plots (d)–(f), and taken at 5 μm from the center for plots (g)–(i).

The CH core density and temperature at a radius of 5 μm, representative of the targets center, are shown in panels (g)–(i). Here the local density and temperature maxima anticipate the respective stagnation times, as they correspond to the moment when the compressing shock reaches the center (i.e., 1.6, 1.7, and 2 ns for, respectively, 0.1, 0.3, and 1 $\mathrm{g/cm^3}$ targets). The temperature at the center can be considerably high, but this corresponds to a very small volume of matter. A second bounce is appreciable in the curves for $\rho_0 = 0.1$ and 0.3 $\mathrm{g/cm^3}$ targets [Figs. 6(g) and 6(h)]. It is due to the shell inertia that is pushing the foam core. After a first shock convergence, the shell itself reaches the center producing a second rise in the density and temperature. In the case of $\rho_0 = 1\,\mathrm{g/cm^3}$, the initial core and shell density being equal, the core is compressed only by the convergence of a shock wave. The maximum central density (temperature) increases (decreases) with the core initial density ρ_0, as expected.

The detailed 2D density and temperature maps obtained for (a) 0.1 $\mathrm{g/cm^3}$, (b) 0.3 $\mathrm{g/cm^3}$, and (c) 1 $\mathrm{g/cm^3}$ targets at their respective stagnation times are shown in Fig. 7. The graphs below the 2D plots represent the corresponding density and temperature profiles along with the cuts at 45°, i.e., the direction of the probing proton or x-ray beams, and also at 0°, i.e., along one of the LP laser beams. Differences between the two profiles are mostly appreciable for $\rho_0 = 0.1\,\mathrm{g/cm^3}$ [Figs. 7(a), 7(d), and 7(g)], where the 2D density and temperature cloverleaf patterns are imprints of the nonisotropic laser irradiation. This is due to the difference between the initial densities of the foam and the shell. For $\rho_0 = 0.3\,\mathrm{g/cm^3}$ this effect is much less visible [Figs. 7(b), 7(e), and 7(h)] and practically nonexistent for $\rho_0 = 1\,\mathrm{g/cm^3}$,

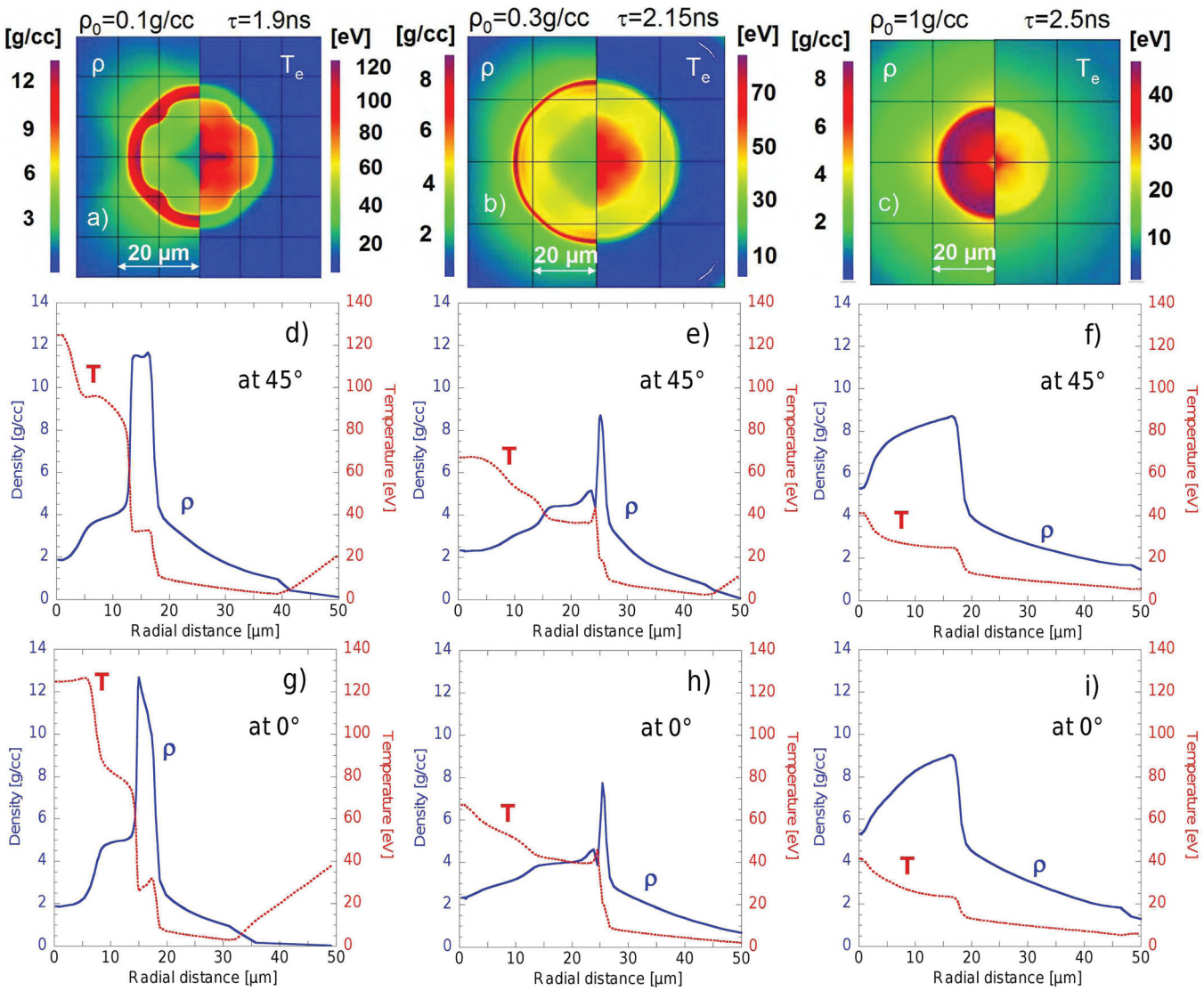

FIG. 7. (Color online) Simulated density and temperature maps of (a) 0.1 g/cm^3, (b) 0.3 g/cm^3, and (c) 1 g/cm^3 targets for 4 × 48 J laser energy at the respective stagnation times 1.9, 2.15, and 2.5 ns. The plots below represent the respective density (blue solid line) and temperature (red dotted line) profiles: Plots (d)–(f) correspond to lineouts of the 2D maps at 45°, i.e., the probing direction, and (g)–(i) at 0° i.e., one of LP laser beams axis.

where the compression is almost isotropic [Figs. 7(c), 7(f), and 7(i)].

The $\rho_0 = 0.1\,\mathrm{g/cm^3}$ target exhibits a ≈15 μm radius region containing a rather low density and high temperature plasma [Fig. 7(a)] issued from the CH core. Here the temperature decreases with radius from 120 eV at the center to 80 eV and the density increases from 2 to 5 g/cm^3. This region is surrounded by a ≈5 μm-thick denser ($\rho \sim 11\,\mathrm{g/cm^3}$) and colder ($T \sim 30\,\mathrm{eV}$) layer, corresponding to the imploded shell. In the outer region appears a rarefaction plasma extended over a few 10 μm and then the underdense, hot coronal plasma where the temperature rises considerably from a radius ∼30 μm.

In the case $\rho_0 = 0.3\,\mathrm{g/cm^3}$, as the foam is denser, the compression is less efficient. The plasma resulting from the CH core is larger, extended up to a ≈25 μm radius. Both core and shell are less compressed than in the previous case. The plasma profiles in the core are less steep, the temperature decreases with radius from 65 to 40 eV, and the density increases from 2.5 to 4.5 g/cm^3. The shell density is smaller with $\rho \sim 8\,\mathrm{g/cm^3}$, its thickness is reduced to a 2 μm thick layer.

In the case $\rho_0 = 1\,\mathrm{g/cm^3}$, the compression is even less efficient. As the core and the shell have the same initial density, the compression is processed differently: In the two previous cases the shell is flying and pushing the foam core, in the present case the core is compressed only by the convergence of a shock wave. One cannot distinguish between plasma regions resulting from the core and the shell. One can see a highly compressed region of ≈20 μm radius with temperature decreasing with radius from 40 to 25 eV and density increasing from 5 to 9 g/cm^3, followed by the rarefaction plasma.

The described CH plasmas obtained at stagnation are represented in an electron density–temperature diagram (n_e, T_e) in Fig. 8(a). They correspond to different plasma states which one can identify to the zones of the diagram separated by the curve $\Gamma = 1/N_{\mathrm{De}} = 1$, Γ representing the plasma coupling parameter and N_{De} the number of electrons in the Debye sphere, and by the curve $E_F/T_e = 1$ where the Fermi energy E_F divided by the temperature is the quantum

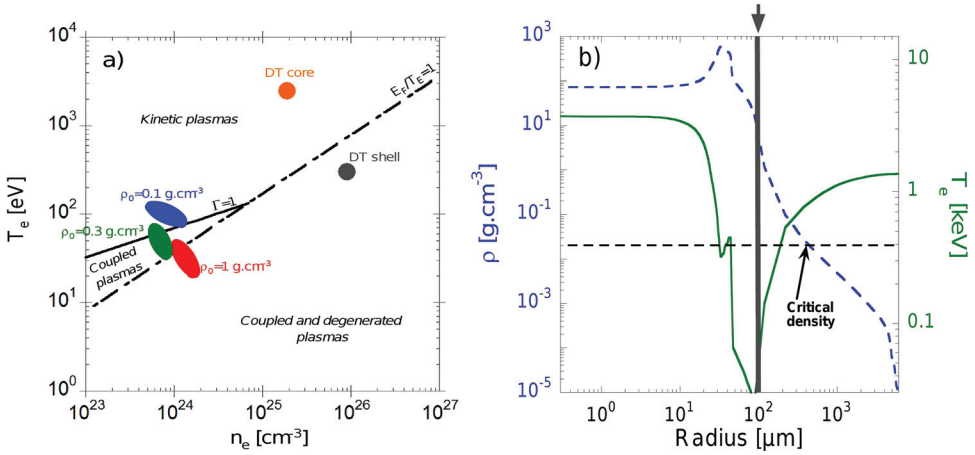

FIG. 8. (Color online) (a) Diagram (n_e, T_e) showing the three different plasma zones obtained at the central region of the cylindrical targets at stagnation according to initial density ρ_0 of the CH core. For comparison are plotted the points representing the required conditions for the compressed DT fuel in the HiPER design for FI. The solid line corresponds to the coupling parameter $\Gamma = 1$ and the dashed line to the quantum degeneracy parameter $E_F/T_e = 1$. (b) Density (dashed blue line) and temperature (solid green line) in the baseline HiPER target at the moment of stagnation $\tau = 11.12$ ns (Refs. 3 and 37). The gray zone (also indicated by the arrow on the top) corresponds to the (ρ, T) range achieved in our cylindrical compression experiment.

degeneracy parameter: The resulting compressed plasmas are kinetic, coupled or coupled and degenerated, respectively, for $\rho_0 = 0.1$, 0.3, and 1 g/cm^3 targets.

In the context of FI studies, these three targets were used in a second phase of the experiment to study the fast electron transport in compressed matter.[26] The fast electrons were generated by the interaction of an intense laser pulse (SP) at normal incidence into the Ni foil at one of the cylinder extremities (see Fig. 1) and propagated along the cylinder axis. The electron transport was studied in the warm and dense plasmas described above. The fast electrons were injected at different stages of the compression by varying the delay between the LP and SP laser beams. It is important to discuss here how the obtained plasmas are suited to fast electron transport studies in the FI scenario. For comparison we plotted in the (n_e, T_e) diagram of Fig. 8(a) two points corresponding to the DT plasmas at stagnation obtained in a simulated implosion of a HiPER baseline target.[3,38] The orange circle corresponds to the 20 μm radius core issued from the DT gas contained in the capsule and the gray circle to the imploded cryogenic DT shell. The plasma density and temperature ranges achieved in our experiment are far from those of the compressed DT designed for FI, but yet we produced plasmas with equivalent coupling and degeneracy parameters. Besides, as one can see in Fig. 8(b), the (ρ, T) range achieved at stagnation in our cylindrical compressions (the region with gray background pointed by the top arrow) corresponds to a region located in the rarefaction plasma between the critical density (where fast electrons are generated) and the compressed shell (where they are supposed to depose their energy to ignite the fuel), at a distance $\approx 60 - 70$ μm from it.

We comment here the difference in the cylindrical implosion of our targets and the spherical ignition designs. In our experiments the fast electrons cross dense plasma zones having radii only slightly bigger than the electron source (15 to 40 μm HWHM). In this case, the radius of the compressed shell exterior surface is only 20 μm and the underdense and hot corona from the ablated material appears at a radius $\sim$35 – 40 μm. The fast electrons propagation will be affected not only by the plasma radial inhomogeneities inside the CH core but also, and probably in a more important way for the $\rho_0 = 0.1$ and 0.3 g/cm^3 targets at stagnation, by the presence of the denser and colder imploding shell, with sharp temperature and density gradients at both interior and exterior shell surfaces perpendicular to the electron propagation direction.

Besides, the structure of the targets is changing with time, so according to the SP beam delay relative to the LP beams (τ), the fast electrons will cross the targets of varying areal density ρL, with L the length of the cylinders. They are injected close to the cylinder axis (within a pointing precision of ± 10 μm) and, therefore, will cross cold and noncompressed material for early times and warm and compressed material for times closer to the respective stagnation time: One can see in Figs. 6(g)–6(i) that the center of the cylinders is still on its initial state for $\tau < 1.6$, <1.7, and <2 ns for, respectively, the $\rho_0 = 0.1$, 0.3, and 1 g/cm^3 cases. This implies that the central zone crossed by the electrons is highly resistive at early times and becomes a conducting plasma behind the convergent shock at later times. At any time there will be radial resistivity gradients at the shock front (before stagnation) and at the target borders. These regions are converging with time and are likely to influence fast electron trajectories, as soon as those gradients appear at distances comparable to the fast electron beam radius.

The results of the fast electron transport and its interpretation are beyond the scope of this paper and will be reported in an upcoming paper.

VI. CONCLUSION

We report on the preparatory phase of an experiment on fast electron transport in warm and dense plasmas. The cylindrically imploded plastic targets were characterized by measuring the target size during compression, by using two diagnostics: x-ray and proton radiography. The experimental data are well reproduced by hydrodynamic simulations coupled to calculations of the proton or x-ray transmission through the imploded targets. Both diagnostics have limitations in spatial resolution. In the case of proton radiography

as described by Volpe,[37] scattering and slowing down of protons in the compressed target induce a reduction of spatial and temporal resolution. The resolution of the x-ray radiography is better because it is not affected by scattering and also the chlorine atoms used as dopants in the target core improve the contrast between the imploded core and the shell. Taking into account the experimental resolution and using 2D hydrodynamic simulations, it is possible to estimate the spatial and temporal temperature and density evolution of the imploding targets. Several target configurations were obtained to test the fast electron transport.[26] The values of density and temperature obtained at stagnation are representative of the plasma domains encountered in FI compressed targets[3,38] at 200 μm beyond the critical density surface, in the fast electron transport region [see Fig. 8(b)]. The plasma conditions created in this experiment allow for more detailed simulations of the fast electron transport due to a better understanding of the physical processes in warm and dense matter.

ACKNOWLEDGMENTS

The authors are thankful to V. T. Tikhonchuk for helpful discussions and comments, to the technical staff of the VULCAN laser facility and also to C. Spindloe and H. Lowe at the RAL target fabrication laboratory, for the target assembling and mounting. This work is supported by the Conseil Regional d'Aquitaine under Project No. 34293, by the European support program Marie Curie IRSES Project No. 230777, and by the HiPER project and Preparatory Phase Funding Agencies (EC, MSMT, and STFC).

[1]M. Tabak, J. Hammer, M. E. Glinsky, X. L. Kruer, S. C. Wilks, J. Woodworth, E. M. Campbell, M. D. Perry, and R. J. Mason, Phys. Plasmas **1**(5), 1626 (1994).
[2]M. Roth, T. E. Cowan, M. H. Key, S. P. Hatchett, C. Brown, W. Fountain, J. Johnson, D. M. Pennington, R. A. Snavely, S. C. Wilks, K. Yasuike, H. Ruhl, F. Pegoraro, S. V. Bulanov, E. M. Campbell, M. D. Perry, and H. Powell, Phys. Rev. Lett. **86**, 436 (2001).
[3]X. Ribeyre, Ph. Nicolaï, G. Schurtz, M. Olazabal-Loumé, J. Breil, P. H. Maire, J. L. Feugeas, L. Hallo, and V. T. Tikhonchuk, Plasma Phys. Controlled Fusion **50**, 025007 (2008); S. Atzeni, A. Schiavi, J. J. Honrubia, X. Ribeyre, G. Schurtz, Ph. Nicolaï, M. Olazabal-Loumé, C. Bellei, R. G. Evans, and J. R. Davies, Phys. Plasmas **15**, 056311 (2008); S. Atzeni, J. R. Davies, L. Hallo, J. J. Honrubia, P. H. Maire, M. Olazabal-Loumé, J. L. Feugeas, X. Ribeyre, A. Schiavi, G. Schurtz, J. Breil, and Ph. Nicolaï, Nucl. Fusion **49**, 055008 (2009).
[4]S. P. Hatchett, D. Clark, M. Tabak, R. E. Turner, C. Stoeckl, R. B. Stephens, H. Shiraga, and K. Tanaka, Fusion Sci. Technol. **49**, 327 (2006).
[5]A. A. Solodov, R. Betti, J. A. Delettrez, and C. D. Zhou, Phys. Plasmas **14**, 062701 (2007).
[6]F. N. Beg, A. R. Bell, A. E. Dangor, C. N. Danson, A. P. Fews, M. E. Glinsky, B. A. Hammel, P. Lee, P. A. Norreys, and M. Tatarakis, Phys. Plasmas **4**(2), 447 (1997).
[7]M. H. Key, M. D. Cable, T. E. Cowan, K. G. Estabrook, B. A. Hammel, S. P. Hatchett, E. A. Henry, D. E. Hinkel, J. D. Kilkenny, J. A. Koch, W. L. Kruer, A. B. Langdon, B. F. Lasinski, R. W. Lee, B. J. MacGowan, A. MacKinnon, J. D. Moody, M. J. Moran, A. A. Offenberger, D. M. Pennington, M. D. Perry, T. J. Phillips, T. C. Sangster, M. S. Singh, M. A. Stoyer, M. Tabak, G. L. Tietbohl, M. Tsukamoto, K. Wharton, and S. C. Wilks, Phys. Plasmas **5**, 1966 (1998).
[8]L. Gremillet, F. Amiranoff, S. D. Baton, J.-C. Gauthier, M. Koenig, E. Martinolli, F. Pisani, G. Bonnaud, C. Lebourg, C. Rousseaux, C. Toupin, A. Antonicci, D. Batani, A. Bernardinello, T. Hall, D. Scott, P. Norreys, H. Bandulet, and H. Pépin, Phys. Rev. Lett. **83**(24), 5015 (1999).
[9]F. Pisani, A. Bernardinello, D. Batani, A. Antonicci, E. Martinolli, M. Koenig, L. Gremillet, F. Amiranoff, S. Baton, J. Davies, T. Hall, D. Scott, P. Norreys, A. Djaoui, C. Rousseaux, P. Fews, H. Bandulet, and H. Pepin, Phys. Rev. E **62**(5), R5927 (2000).
[10]K. Yasuike, M. H. Key, S. P. Hatchett, R. A. Snavely, and K. B. Wharton, Rev. Sci. Instrum. **72**(1), 1236 (2001).
[11]J. J. Santos, F. Amiranoff, S. D. Baton, L. Gremillet, M. Koenig, E. Martinolli, M. Rabec Le Gloahec, C. Rousseaux, D. Batani, A. Bernardinello, G. Greison, and T. Hall, Phys. Rev. Lett. **89**, 025001 (2002).
[12]R. B. Stephens, R. A. Snavely, Y. Aglitskiy, F. Amiranoff, C. Andersen, D. Batani, S. D. Baton, T. Cowan, R. R. Freeman, T. Hall, S. P. Hatchett, J. M. Hill, M. H. Key, J. A. King, J. A. Koch, M. Koenig, A. J. MacKinnon, K. L. Lancaster, E. Martinolli, P. Norreys, E. Perelli-Cippo, M. Rabec Le Gloahec, C. Rousseaux, J. J. Santos, and F. Scianitti, Phys. Rev. E **69**, 066414 (2004).
[13]E. Martinolli, M. Koenig, S. D. Baton, J. J. Santos, F. Amiranoff, D. Batani, E. Perelli-Cippo, F. Scianitti, L. Gremillet, R. Mélizzi, A. Decoster, C. Rousseaux, T. A. Hall, M. H. Key, R. Snavely, A. J. MacKinnon, R. R. Freeman, J. A. King, R. Stephens, D. Neely, and R. J. Clarke, Phys. Rev. E **73**, 046402 (2006).
[14]J. J. Santos, A. Debayle, Ph. Nicolaï, V. T. Tikhonchuk, M. Manclossi, D. Batani, A. Guemnie-Tafo, J. Faure, V. Malka, and J. J. Honrubia, Phys. Plasmas **14**, 103107 (2007).
[15]J. S. Green, V. M. Ovchinnikov, R. G. Evans, K. U. Akli, H. Azechi, F. N. Beg, C. Bellei, R. R. Freeman, H. Habara, R. Heathcote, M. H. Key, J. A. King, K. L. Lancaster, N. C. Lopes, T. Ma, A. J. MacKinnon, K. Markey, A. McPhee, Z. Najmudin, P. Nilson, R. Onofrei, R. Stephens, K. Takeda, K. A. Tanaka, W. Theobald, T. Tanimoto, J. Waugh, L. Van Woerkom, N. C. Woolsey, M. Zepf, J. R. Davies, and P. A. Norreys, Phys. Rev. Lett. **100**, 015003 (2008).
[16]F. Perez, S. D. Baton, M. Koenig, C. D. Chen, D. Hey, M. H. Key, S. Le Pape, T. Ma, H. S. McLean, A. G. MacPhee, P. K. Patel, Y. Ping, F. N. Beg, D. P. Higginson, C. W. Murphy, H. Sawada, B. Westover, T. Yabuuchi, K. U. Akli, E. Giraldez, M. Hoppe, Jr., C. Shearer, R. B. Stephens, L. Gremillet, E. Lefebvre, R. R. Freeman, G. E. Kemp, A. G. Krygier, L. D. Van Woerkom, R. Fedosejevs, R. H. Friesen, Y. Y. Tsui, and D. Turnbull, Phys. Plasmas **17**, 113106 (2010).
[17]S. Kar, A. P. L. Robinson, D. C Carroll, O Lundh, K. Markey, P. McKenna, P. Norreys, and M. Zepf, Phys. Rev. Lett. **102**, 055001 (2009).
[18]T. A. Hall, S. Ellwi, D. Batani, A. Bernardinello, V. Masella, M. Koenig, A. Benuzzi, J. Krishnan, F. Pisani, A. Djaoui, P. Norreys, D. Neely, S. Rose, M. H. Key, and P. Fews, Phys. Rev. Lett. **81**, 1003 (1998).
[19]D. Batani, J. R. Davies, A. Bernardinello, F. Pisani, M. Koenig, T. A. Hall, S. Ellwi, P. Norreys, S. Rose, A. Djaoui, and D. Neely, Phys. Rev. E **61**(5), 5725 (2000).
[20]J. J. Santos, D. Batani, P. McKenna, S. D. Baton, F. Dorchies, A. Dubrouil, C. Fourment, S. Hulin, Ph. Nicolaï, M. Veltcheva, P. Carpeggiani, M. N. Quinn, E. Brambrink, M. Koenig, M. Rabec Le Glohaec, Ch. Spindloe, and M. Tolley, Plasma Phys. Controlled Fusion **51**, 014005 (2009)
[21]J. Pasley, M. Wei, E. Shipton, S. Chen, T. Ma, F. N. Beg, N. Alexander, R. Stephens, A. G. MacPhee, D. Hey, S. Le Pape, P. Patel, A. Mackinnon, M. Key, D. Offermann, A. Link, E. Chowdhury, L. Van-Woerkom, and R. R. Freeman, Phys. Plasmas **14**, 120701 (2007).
[22]T. Ma, M. H. Key, R. J. Mason, K. U. Akli, R. L. Daskalova, R. R. Freeman, J. S. Green, K. Highbarger, P. A. Jaanimagi, J. A. King, K. L. Lancaster, S. P. Hatchett, A. J. Mackinnon, A. G. MacPhee, P. A. Norreys, P. K. Patel, R. B. Stephens, W. Theobald, L. D. V. Woerkom, M. S. Wei, S. C. Wilks, and F. N. Beg, Phys. Plasmas **16**, 112702 (2009)
[23]J. J. Santos, D. Batani, P. McKenna, S. D. Baton, F. Dorchies, A. Dubrouil, C. Fourment, S. Hulin, E. d'Humières, Ph. Nicolaï, L. Gremillet, A. Debayle, J. J. Honrubia, P. Carpeggiani, M. Veltcheva, M. N. Quinn, E. Brambrink, and V. Tikhonchuk, J. Phys.: Conf. Ser. **244**, 022060 (2010)
[24]H. Nakamura, Y. Sentoku, T. Matsuoka, K. Kondo, M. Nakatsutsumi, T. Norimatsu, H. Shiraga, K. A. Tanaka, T. Yabuuchi, and R. Kodama, Phys. Rev. Lett. **100**, 165001 (2008).
[25]W. W. Hsing, Cris W. Barnes, J. B. Beck, N. M. Hoffman, D. Galmiche, A. Richard, J. Edwards, P. Graham, S. Rothman, and B. Thomas, Phys. Plasmas **4**(5), 1832 (1997).
[26]F. Perez, M. Koenig, D. Batani, S. D. Baton, F. N. Beg, C. Benedetti, E. Brambrink, S. Chawla, F. Dorchies, C. Fourment, M. Galimberti, L. A. Gizzi, R. Heathcote, D. P. Higginson, S. Hulin, R. Jafer, P. Koester, L. Labate, K. Lancaster, A. J. MacKinnon, A. G. McPhee, W. Nazarov, Ph. Nicolaï, J. Pasley, A. Ravasio, M. Richetta, J. J. Santos, A. Sgattoni, C. Spindloe, B. Vauzour, and L. Volpe, Plasma Phys. Controlled Fusion **51**, 124035 (2009).
[27]B. Vauzour, J. J. Santos, D. Batani, S. D. Baton, M. Koenig, Ph. Nicolaï, F. Perez, F. N. Beg, C. Benedetti, R. Benocci, E. Brambrink, S. Chawla,

M. Coury, F. Dorchies, C. Fourment, M. Galimberti, L. A. Gizzi, R. Heathcote, D. P. Higginson, J. J. Honrubia, S. Hulin, R. Jafer, L. C. Jarrot, L. Labate, K. Lancaster, P. Koester, A. J. MacKinnon, P. McKenna, A. G. McPhee, W. Nazarov, J. Pasley, R. Ramis, Y. Rhee, C. Regan, X. Ribeyre, M. Richetta, F. Serres, H.-P. Schlenvoigt, G. Schurtz, A. Sgattoni, C. Spindloe, X. Vaisseau, L. Volpe, and V. Yahia, Nucl. Instrum. Methods A (2010).

[28]P. H. Maire, R. Abgrall, J. Breil, and J. Ovadia, SIAM J. Sci. Comput. **29**(4), 1781 (2007).

[29]P. H. Maire and J. Breil, Int. J. Numer. Methods Fluids **56**, 1161 (2008).

[30]Y. Agliskiy, T. Lehecka, S. Obenschain, S. Bodner, C. Pawley, K. Gerber, J. Sethian, C. M. Brown, J. Seely, U. Feldman, and G. Holland, Appl. Opt. **37**(22), 5253 (1998).

[31]A. Benuzzi-Mounaix, B. Loupias, M. Koenig, A. Ravasio, N. Ozaki, M. Rabec le Gloahec, T. Vinci, Y. Aglitskiy, A. Faenov, T. Pikuz, and T. Boehly, Phys. Rev. E **77**(4), 045402(R) (2008).

[32]J. A. Koch, Y. Aglitskiy, C. Brown, T. Cowan, R. Freeman, S. Hatchett, G. Holland, M. Key, A. MacKinnon, J. Seely, R. Snavely, and R. Stephens, Rev. Sci. Instrum. **74**(3), 2130 (2003).

[33]M. Borghesi, D. H. Campbell, A. Schiavi, M. G. Haines, O. Willi, A. J. MacKinnon, P. Patel, L. A. Gizzi, M. Galimberti, R. J. Clarke, F. Pegoraro, H. Ruhl, and S. Bulanov, Phys. Plasmas **9**(5), 2214 (2002).

[34]S. Kar, M. Borghesi, P. Audebert, A. Benuzzi-Mounaix, T. Boehly, D. Hicks, M. Koenig, K. Lancaster, S. Lepape, A. Mackinnon, P. Norreys, P. Patel, and L. Romagnani, High Energy Density Phys. **4**, 26 (2008).

[35]R. M. More, K. H. Warren, D. A. Young, and G. B. Zimmerman, Phys. Fluids **31**, 3059 (1988).

[36]See SESAME Report on the Los Alamos Equation-of-State Library, LANL Report No. LALP-83-4 (T4 Group LANL, Los Alamos, 1983).

[37]L. Volpe, D. Batani, B. Vauzour, Ph. Nicolai, J. J. Santos, C. Regan, A. Morace1, F. Dorchies, C. Fourment, S. Hulin, M. Koenig, F. Perez, S. Baton, K. Lancaster, M. Galimberti, R. Heathcote, M. Tolley, Ch. Spindloe, P. Koester, L. Labate, L. A. Gizzi, C. Benedetti, A. Sgattoni, M. Richetta, J. Pasley, F. Beg, S. Chawla, D. P. Higginson, A. MacKinnon, and A. G. MacPhee, Phys. Plasmas **18**, 006101 (2011); L. Volpe, R. Jafer, B. Vauzour, Ph. Nicolaï, J. J. Santos, F. Dorchies, C. Fourment, S. Hulin, C. Regan, F. Perez, S. Baton, K. Lancaster, M. Galimberti, R. Heathcote, M. Tolley, Ch. Spindloe, W. Nazarov, P. Koester, L. Labate, L. A. Gizzi, C. Benedetti, A. Sgattoni, M. Richetta, J. Pasley, F. N. Beg, S. Chawla, D. P. Higginson, A. G. MacPhee, and D. Batani, Plasma Phys. Control. **53**, 032003 (2011).

[38]V. T. Tikhonchuk, T. Schlegel, C. Regan, M. Temporal, J.-L. Feugeas, Ph. Nicolaï, and X. Ribeyre, Nucl. Fusion **50**, 045003 (2010).